

Dynamical Modelling of the Remarkable Four-Armed Barred Spiral Galaxy ESO 566-24

P. Rautiainen – University of Oulu

H. Salo – University of Oulu

R. Buta – University of Alabama

Deposited 07/31/2019

Citation of published version:

Rautiainen, P., Salo, H., Buta, R. (2004): Dynamical Modelling of the Remarkable Four-Armed Barred Spiral Galaxy ESO 566-24. *Monthly Notices of the Royal Astronomical Society*. 349(3). DOI: <https://doi.org/10.1111/j.1365-2966.2004.07561.x>

Dynamical modelling of the remarkable four-armed barred spiral galaxy ESO 566–24

P. Rautiainen,¹* H. Salo¹ and R. Buta²

¹*Department of Physical Sciences, University of Oulu, PO Box 3000, FIN-90014 Oulun yliopisto, Finland*

²*Department of Physics and Astronomy, University of Alabama, Box 870324, Tuscaloosa, AL 35486, USA*

Accepted 2003 December 17. Received 2003 December 10; in original form 2003 May 23

ABSTRACT

ESO 566–24 is an extraordinary barred galaxy that has four regularly spaced spiral arms in blue light images. This type of spiral structure, which is rare among the spiral population, is also clearly seen in near-infrared (NIR) images, and thus is present in the old stellar population. We have constructed dynamical models of ESO 566–24. The gravitational potential is determined using NIR photometry, and the gas dynamics is modelled as inelastically colliding particles. The resulting morphology and kinematics with different assumed pattern speeds, disc vertical thicknesses and dark halo contributions are compared with observations. Our models reproduce the main morphological features of this galaxy: the four-armed spiral, and the inner and nuclear rings. The pattern speed of the bar is such that the corotation resonance is well outside the bar radius, $r_{\text{CR}}/r_{\text{b}} = 1.6 \pm 0.3$. The four-armed spiral resides in the region between inner and outer 4/1 resonances. In addition, the main kinematical features, including bar-induced deviations from circular rotation, are explained by our models. The best fit is obtained when the dark halo contribution is just enough to make the modelled rotation curve match the observed one. Thus, luminous matter dominates the rotation curve within the disc region.

Key words: galaxies: evolution – galaxies: fundamental parameters – galaxies: individual: ESO 566–24 – galaxies: kinematics and dynamics – galaxies: spiral – galaxies: structure.

1 INTRODUCTION

When observed in the near-infrared (NIR), about 70 per cent of disc galaxies have a bar (Eskridge et al. 2000; Knapen, Shlosman & Peletier 2000). Barred galaxies often have rings or pseudo-rings in their discs with very distinctive characteristics (Buta & Combes 1996). Depending on its relative size with respect to the bar radius, r_{b} , a ring can be classified as an outer ring (semimajor axis $a_{\text{r}} \approx 2.2 r_{\text{b}}$), an inner ring ($a_{\text{r}} \approx r_{\text{b}}$) or a nuclear ring ($a_{\text{nr}} \approx 0.1 r_{\text{b}}$) (Buta & Crocker 1993). Although all three types of barred galaxy rings can show enhanced star formation (see, e.g. Buta & Purcell 1998), nuclear rings are most prone to starbursts (Maoz et al. 1996; Buta & Combes 2000). Barred spiral galaxies can also show offset dust lanes on the leading sides of the bar (assuming trailing spiral arms).

In most studies, large-scale bars are suggested to be fast rotators, i.e. their corotation resonance (CR) radius is near the end of the bar (e.g. Sellwood 1981; Athanassoula 1992). This can set limitations to a dark halo density inside the disc region. It has been suggested that the interaction between a bar and a centrally concentrated halo decelerates strongly the bar rotation (Weinberg 1985; Debattista &

Sellwood 1998, 2000). Thus, fast rotating bars could imply that the halo contribution is negligible in the inner parts of the disc. However, the high angular momentum transfer rate between the bar and the dark halo may not be inevitable (Valenzuela & Klypin 2003; Athanassoula 2003).

In principle, the pattern speed of a bar, Ω_{b} , can be determined from observations for a disc with a well-defined pattern speed (Tremaine & Weinberg 1984). The Tremaine–Weinberg method further assumes that the used tracer component follows the continuity equation, i.e. its intensity is proportional to total density. When these conditions are fulfilled, Ω_{b} can be determined from the observed intensity and the line-of-sight velocity along a strip parallel to the major axis of the galaxy. In most of the cases, where this method has been applied, the CR seems to be near the end of the bar (Kent 1987; Merrifield & Kuijken 1995; Aguerri, Debattista & Corsini 2003). Note, however, that owing to its limitations, this method has been successfully applied mostly to SBO galaxies.

Another kinematical method to determine the pattern speed was presented by Canzian (1993) and is based on observed residuals in the velocity field after subtracting the axisymmetric velocity component. In the case of a two-armed spiral, the velocity residuals should exhibit an $m = 1$ spiral shape inside corotation and an $m = 3$ spiral outside CR. This method was used to determine the pattern speed in NGC 4321 (Sempere et al. 1995; Canzian & Allen 1997), giving

*E-mail: pertti.rautiainen@oulu.fi

a rather low value, which sets $r_{\text{CR}} = 1.6\text{--}1.8r_{\text{b}}$. However, the method is very sensitive to noise, and the construction of the axisymmetric velocity component is not trivial. Purcell (1998), who studied a larger galaxy sample, found that only in seven of 27 Sbc galaxies could the expected pattern be seen in velocity field residuals.

There are several suggested resonance indicators related to morphological details of spiral structure (Elmegreen, Seiden & Elmegreen 1989). Even if these are valid, their application to barred galaxies can be problematic: there may be more than one mode in the system. For example the outer spiral arms can have a lower pattern speed than the bar (Sellwood & Sparke 1988). In such cases the pattern speed derived, for example, from the dust-lane morphology of the outer arms would not correspond to that of the bar.

The formation of rings in barred galaxies has been explained by the response of the dissipative gas component to the gravitational torque of the bar (Schwarz 1981; Combes & Gerin 1985; Byrd et al. 1994; Buta & Combes 1996). The shapes of the rings resemble closed periodic orbits in barred potentials (Contopoulos & Grosbøl 1989). When the non-axisymmetric perturbation is weak, the outer rings form near the outer Lindblad resonance (OLR), the inner rings near the inner 4/1 resonance and the nuclear rings near the inner Lindblad resonance (ILR). Using a known rotation curve, the sizes of the rings can be used to estimate Ω_{b} . However, in barred galaxies the linear approximation is not valid, and the application of results based on it is not unambiguous. Furthermore, in addition to the main bar, rings can be affected by another mode (Rautiainen & Salo 2000; Rautiainen, Salo & Laurikainen 2002).

The effect of the strength of the bar is taken into account when detailed models for individual galaxies are constructed. The adopted approach has varied from fitting an analytical mass model to observations (Duval & Athanassoula 1983) to determining the mass model from NIR observations (Lindblad, Lindblad & Athanassoula 1996; Lindblad & Kristen 1996). The number of successfully modelled barred galaxies is still quite small, and it is not clear how well the ranges of parameters such as the pattern speed and the relative strength of the non-axisymmetric perturbation are known.

We started our modelling project of ringed galaxies with the normal, but rather weakly barred galaxy IC 4214. From the observations (Buta et al. 1999), we constructed a model with a few free parameters (Salo et al. 1999). In our best-fitting models both the morphology and kinematics were well reproduced. Here we extend our studies by constructing a dynamical model for an extraordinary barred spiral: the four-armed galaxy ESO 566–24. We use numerical models to find the parameter range which can reproduce the regular four-armed morphology of ESO 566–24. We study how resonances are located with respect to the observed structures such as rings, and we also identify some of the orbits supporting these structures.

2 A REMARKABLE FOUR-ARMED BARRED SPIRAL

ESO 566–24 is a barred spiral galaxy of de Vaucouleurs revised Hubble type SB(r)b. It was first recognized as being an exceptional example of a four-armed ringed barred spiral galaxy during early stages in the production of the Catalog of Southern Ringed Galaxies (CSRG, Buta 1995). High-quality optical CCD images obtained in follow-up work by Buta & Crocker (1991), reveal an extremely regular four-armed pattern of normal spiral arms, as well as star formation in the inner ring and in a previously unknown nuclear ring. Regular four-armed outer spirals are very rare and, if seen at all, appear in a partial manner, as the secondary spiral arcs and two main outer arms seen in NGC 1433 (Buta 1986; Buta et al. 2001).

ESO 566–24 has a clear bar component in both visual and NIR images. Applying several methods to the H -band image: for example, axis ratios of isophotes and local amplitude minima of $m = 2$ and $m = 4$ Fourier components of disc surface brightness, we estimate that $r_{\text{b}} = 18 \pm 2$ arcsec, or about 1.6 times the exponential scalelength of the disc, $h_{\text{r}} \approx 11.3$ arcsec. This is in reasonable agreement with the value adopted in Buta et al. (1998), $r_{\text{b}} = 16.7$ arcsec. Colour index maps, for example, $B - I$, show that there are dust lanes on the leading sides of the bar (Buta & Crocker 1991). The bar is surrounded by an inner ring, which can be seen also in the H -band image. The ring appears circular in the plane of the sky but deprojects to an ellipse parallel with the bar major axis for the adopted orientation parameters: position angle $\text{PA} = 73^\circ$, and inclination $i = 43^\circ$ (Buta et al. 1998). Parallel alignment is a normal characteristic of barred galaxy inner rings (Buta 1995). The deprojected semimajor axis radius of the inner ring is about 19 arcsec. There is also a nuclear ring with a semimajor axis radius of about 4 arcsec.

The four bright spiral arms extend between 20 and 40 arcsec. The arms start from the inner ring, two from its major axis and the other two from the minor axis. The arms have about the same strength and length in the NIR H -band image. At about 35 arcsec the arm–interarm contrast is almost as high as 2 (~ 0.7 mag). Such high values in NIR images have been found only in a few galaxies, such as M 51 (Rix & Rieke 1993). There is also a single outer spiral arm or a partial outer ring, that is not connected to the four-armed spiral (Buta et al. 1998). Fig. 1 shows B - and H -band images of ESO 566–24.

The rotation curve inferred from the velocity field (see Fig. 2) has a peculiar shape: in the inner parts it rises steeply, then it has a short flat part at ~ 120 km s $^{-1}$. Outside this area, it rises steeply again to the peak value, after which it quickly drops to the constant level of ~ 190 km s $^{-1}$. The peculiar inner rotation curve is probably at least partly caused by non-circular motions induced by the bar, as axisymmetric rotation curves constructed from any realistic combinations of bulge, disc and halo cannot produce such a structure. The zero-velocity curve of the velocity field implies the presence of non-circular motion, but the effect is weak because the orientation of the bar is almost perpendicular to the line of nodes, and hence little of the radial component of the velocity vector projects to the line of sight (see also Buta 1988).

3 METHODS

We estimate the mass distribution from NIR H -band photometry, assuming a constant mass-to-light ratio throughout the disc. First a bulge–disc decomposition is carried out, and the resulting bulge component is subtracted from the image before deprojection. Then the disc surface brightness (and surface density) distribution is approximated using a Fourier decomposition

$$\begin{aligned} \Sigma(r, \theta) &= \Sigma_0(r) \left\{ 1 + \sum_{m=1}^{\infty} A_m(r) \cos [m(\theta - \theta_m)] \right\} \\ &= \Sigma_0(r) + \sum_{m=1}^{\infty} \Sigma_m(r, \theta), \end{aligned} \quad (1)$$

where r and θ are the polar coordinates, $\Sigma(r, \theta)$ the disc surface density, Σ_0 the axisymmetric surface density, and $A_m(r)$ and $\theta_m(r)$ are the Fourier amplitude and phase angles. For our analysis, we used even components $m = 0\text{--}8$. This smoothes small-scale structures such as star forming regions but has little or no impact on the basic background stellar potential. From the density components Σ_m , we

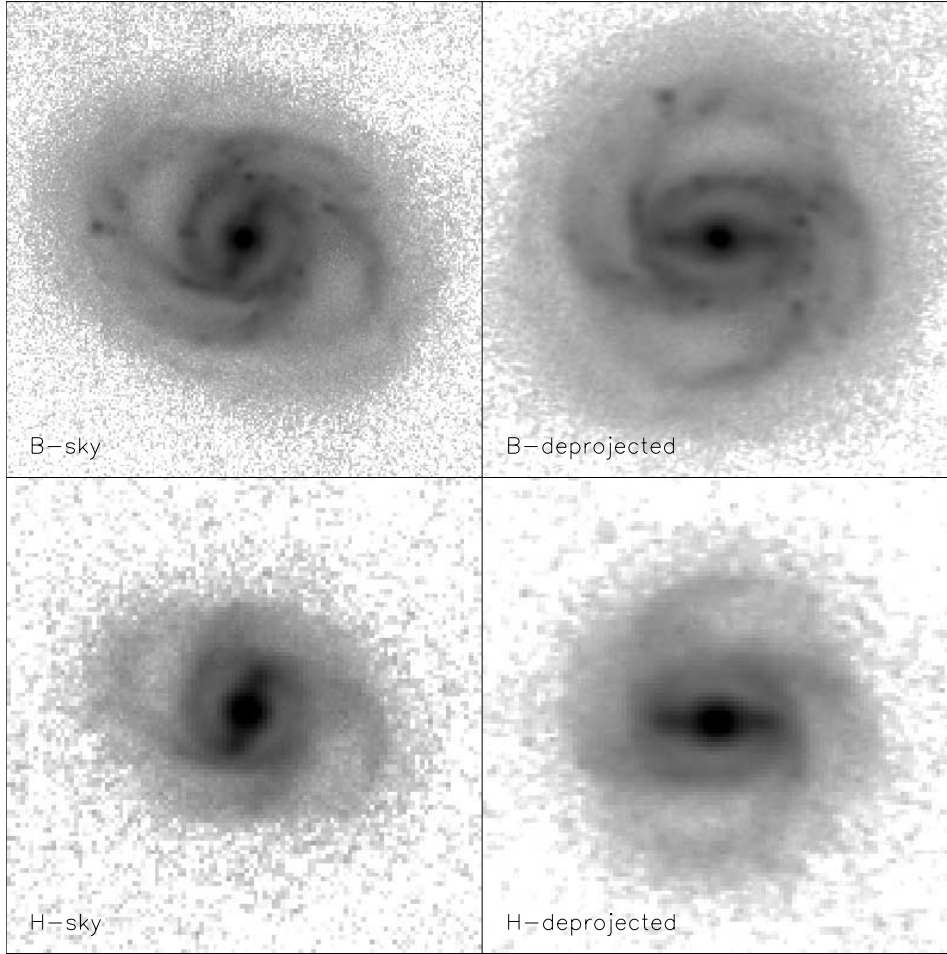


Figure 1. *B*- and *H*-band images of ESO 566–24. The images on the left-hand side show the galaxy as it is oriented on the sky (foreground stars have been removed) and the images on the right-hand side have been first deprojected and then rotated so that the bar is horizontal. The width of the frames is 120 arcsec.

then calculate the potential components Φ_m

$$\Phi_m(r, \theta, z = 0) = -G \int_0^\infty r' dr' \int_0^{2\pi} \Sigma_m(r', \theta') g(\Delta r) d\theta', \quad (2)$$

where $(\Delta r)^2 = r'^2 + r^2 - 2rr' \cos(\theta' - \theta)$ and the convolution function,

$$g(\Delta r) = \int_{-\infty}^{\infty} \varrho_z(z) [(\Delta r)^2 + z^2]^{-1/2} dz, \quad (3)$$

is used for calculating the effect of the vertical density profile $\varrho(z)$ (normalized to unity when integrated over the vertical direction). In Salo et al. (1999) the gravity softening was used as a measure of finite disc thickness. In this study we use an exponential vertical distribution,

$$\varrho(z) = \frac{1}{2h_z} \exp(-|z|/h_z), \quad (4)$$

which has a similar effect. A more detailed description of the potential calculation can be found in Laurikainen & Salo (2002). We have tried scaleheights in the range of 1/12–1/2 times the radial exponential scalelength h_r of the disc, corresponding to the change from a very thin disc to an unrealistically thick one; for the morphological type of ESO 566–24, $h_z/h_r \approx 1/6$ is expected (de Grijs, Peletier & van der Kruit 1997; de Grijs 1998).

The gas component is modelled as a two-dimensional disc consisting of 20 000 inelastically colliding test particles. In each collision, the relative velocity component parallel with the line joining the particle centres is reversed and multiplied by the coefficient of restitution, $0 \leq \alpha < 1$. Our standard value is $\alpha = 0$, but we also made some tests with other values. In each time-step, only one collision per particle is allowed. The particle motion is integrated using leap-frog integration. The time-step is chosen so that at the radius of the smallest morphological detail, the nuclear ring, one circular rotation period is about 50 steps. In addition to gas particles, we have also made simulations with 200 000 non-colliding ‘stellar’ particles with different initial velocity dispersions. These are used as a tracer of the orbital structure. For more details on the simulation code, see Salo et al. (1999).

The non-axisymmetric perturbation of the potential is turned on gradually during four bar rotation periods. This procedure was adopted to smoothly guide particles to realistic orbits, thus trying to minimize the effect of transient phenomena related to abrupt changes in the potential, for example, a large number of gas particles ending up on crossing orbits.

We use a modified version of the bulge model presented in Buta et al. (1998). We take the average radial profile of the bulge, assume the bulge to be axisymmetric and calculate its gravitational potential using the algorithm described in Kent (1986). As a halo component

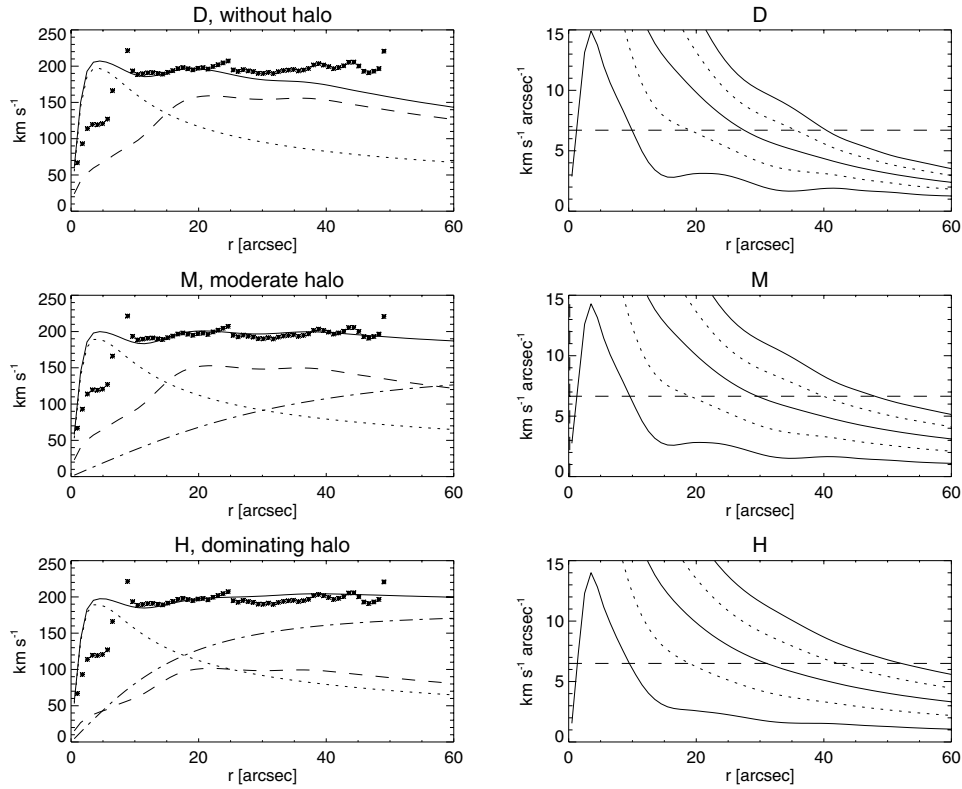


Figure 2. Comparison between three different mass models (see Table 1). The frames on the left-hand side show the rotation curves, total rotation curve indicated as a continuous line, and the contributions from the bulge as a dotted line, the disc as a dashed line and the halo as a dash-dotted line. The asterisk symbols show circular velocities determined from the observed velocity field. The frames on the right-hand side show Ω (thick continuous line), $\Omega \pm \kappa/2$ (thin continuous lines) and $\Omega \pm \kappa/4$ (dotted lines). The dashed horizontal line shows the pattern speed at which the semimajor axis of the inner ring (19 arcsec) coincides with the inner 4/1 resonance.

we use an isothermal sphere with a constant core radius, which has a rotation curve

$$v_h(r) = v_\infty \sqrt{\frac{r^2}{r^2 + r_c^2}}, \quad (5)$$

where v_∞ is the asymptotic velocity at infinity and r_c is the core radius.

4 MODELLING

We have constructed three major sets of models: series D without a halo component, series M with a moderate halo and series H with a dominating halo (see Table 1). The M/L ratios of the bulge and disc were chosen to be such that the rotation amplitude at 20 arcsec corresponds with the observed one. In all series, we have varied several parameters such as the bar pattern speed and the disc thickness.

The left-hand frames of Fig. 2 compare the rotation curves of models of series D (no halo), M (moderate halo) and H (dominating halo) with a similar disc thickness ($h_z/h_r = 1/6$). Also shown are the circular velocity points determined from the observed velocity field using the method presented by Warner, Wright & Baldwin (1973). If we adopt the definition of a maximal disc (or disc + bulge) by Sackett (1997): a disc is maximal if its rotation speed at radius $r_{2.2} = 2.2 h_r$ is 75–95 per cent of the total circular speed at this radius, then our moderate halo series M resides near the lower limit of maximal discs. Perhaps a better name would be a minimum halo model: only such an amount of halo was included that is needed to make the outer

Table 1. The main parameters for the three model families D, M and H. The H -band mass–luminosity ratios of the bulge $(M/L)_B$ and the disc $(M/L)_D$ are given in solar units, assuming $M_{H\odot} = 3.37$ and the distance being 45 Mpc. Also listed are the parameters determining the halo rotation curve: velocity in infinity, v_∞ in km s^{-1} , and core radius, r_c , in arcsec.

Model family	$(M/L)_B$	$(M/L)_D$	v_∞	r_c
D	1.3	1.3		
M	1.2	1.2	152	40.0
H	1.2	0.54	180	20.0

curve as flat as the observed rotation curve. This halo component is quite close to prediction from the ‘universal rotation curve’ (URC; Persic, Salucci & Stel 1996). When using the adopted distance and orientation parameters, the difference between the URC and model M haloes is less than 10 km s^{-1} inside the optical radius, R_{opt} (here taken to be $D_{25}/2 \approx 48.7$ arcsec).

The right-hand frames of Fig. 2 show the corresponding ‘frequency diagrams’, i.e. curves showing Ω , $\Omega \pm \kappa/2$ and $\Omega \pm \kappa/4$, where Ω is the circular frequency and κ is the epicyclic frequency. The inner parts of the models have very similar rotation curves, and thus with the same pattern speed, the inner resonance distances (ILRs and inner 4/1 resonance) would be about the same. Alternatively, the outer resonance radii are different. For example, the distance between the inner and outer 4/1 resonances is larger in

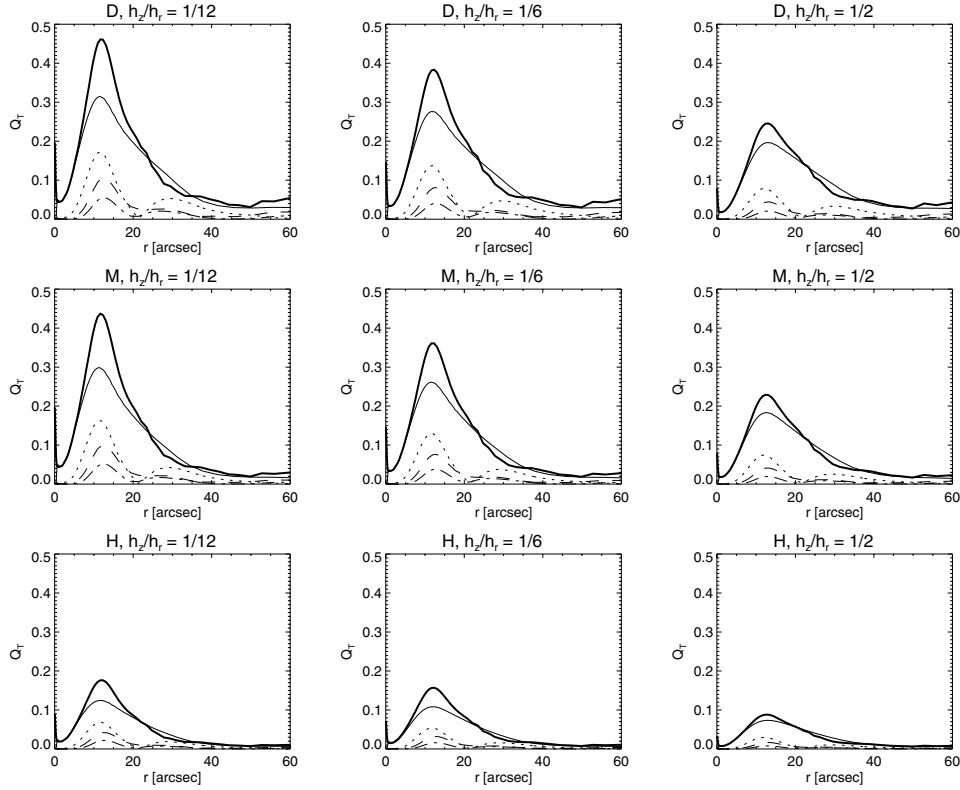


Figure 3. The relative tangential force in models without a halo (top row), with a moderate halo (middle row) and with a strong halo (bottom row). The thick continuous line shows the maximum force, whereas the $m = 2$ component is indicated with a thin continuous line, $m = 4$ component with a dotted line, $m = 6$ with a dashed line and $m = 8$ with a dot-dashed line. Note that owing to phase differences, the maximum is less than the sum of the amplitudes of the different components.

models with a halo than in models without one. Throughout this article we use $\text{km s}^{-1} \text{arcsec}^{-1}$ as a unit of pattern speed. We denote models of each mass model series with the pattern speed: for example model D6.7 is a series D model with pattern speed $\Omega_b = 6.7 \text{ km s}^{-1} \text{arcsec}^{-1}$. At the adopted distance of 45 Mpc, $1 \text{ km s}^{-1} \text{arcsec}^{-1}$ corresponds to about $4.6 \text{ km s}^{-1} \text{kpc}^{-1}$ and the length of a simulation is about 2.7 Gyr (about 14 bar rotation periods in our best-fitting case).

4.1 The effect of model parameters

4.1.1 The effect of disc thickness

We have made simulations with a range of the disc scaleheight from 1/12 to 1/2. In Fig. 3 we show the Fourier components of the tangential force relative to the axisymmetric radial force (total of bulge, disc and halo) as a function of radius for different mass models. The $m = 2$ component has one maximum, at about 12 arcsec, well inside the bar. The $m = 4$ component has two clear maxima, one coinciding with the $m = 2$ maximum, and the other broader one in about the middle of the four-armed spiral structure. The $m = 6$ and $m = 8$ components also have two maxima, the inner coinciding with the $m = 2$ maximum, and the outer ones being inside the outer $m = 4$ maximum.

As a measure of bar strength, we use the relative tangential force Q_T (Combes & Sanders 1981)

$$Q_T(r) = F_T^{\max}(r) / \langle F_R(r) \rangle, \quad (6)$$

where $F_T^{\max}(r)$ is the maximum of the tangential force at a given radius r , and $\langle F_R(r) \rangle$ is the azimuthally averaged radial force at the

same radius. The maximum of $Q_T(r)$ over radius, or Q_b , has been used as a single measure of bar strength by Buta & Block (2001) and Laurikainen, Salo & Rautiainen (2002). In our basic mass models, the extreme values of the Q_b parameter vary from 0.1 to 0.47 when going from the thickest disc models of series H to the thinnest disc models of series D. In each mass model series, the models with the thinnest discs have about twice as strong bars as models with the thickest discs if measured by Q_b . The effect of disc thickness on Q_T is much weaker in the region of the spiral arms.

In Fig. 4 we show the effect of disc thickness on the simulated gas morphology. When comparing with the observed four-armed spiral of ESO 566–24, we see that in the D series the fit is best when the disc is very thick ($h_z/h_r = 1/2$). In series M, the best fit is obtained with a thinner disc (both $h_z/h_r = 1/12$ and $h_z/h_r = 1/6$ give a fairly good fit). In series H, the spiral response to the potential is always too weak. This can be explained by the weakness of the non-axisymmetric perturbation at the spiral region: it is less than half of that in series M and D. We can also see that the size of the nuclear ring depends on the disc thickness: a thicker disc leads to a larger ring owing to the reduced non-axisymmetric perturbation at its location, shifting the ring closer to a linear ILR. The axial ratio of the inner ring is not very sensitive to Q_b , which is not surprising, because the location where the maximum of Q_T is reached is well inside the ring. At the ring region, Q_T varies less than its maximum value Q_b when compared in models with different disc scaleheights.

4.1.2 The effect of pattern speed

For each basic mass model, we ran a series of simulations with five different pattern speeds. The middle pattern speed of each series was

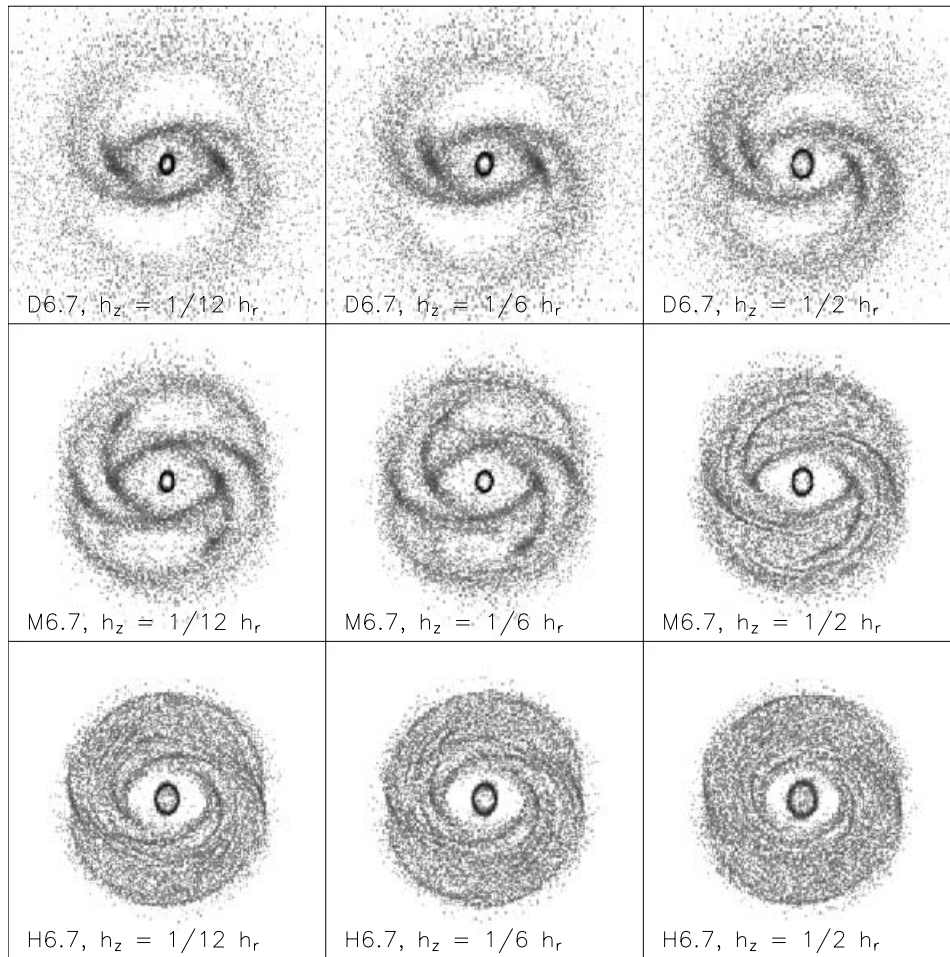


Figure 4. The effect of the disc thickness in models from the disc-dominated series D (top row), series M with a moderate halo (middle row) and the halo-dominated series H (bottom row). This is compared with Fig. 3 which shows the strength of the non-axisymmetric force field in each case. The width of the frames is 120 arcsec. The models are shown one bar period after the bar has reached its full strength.

chosen so that the semimajor axis radius of the inner ring coincides with the inner 4/1 resonance, and the highest pattern speed so that its corotation radius is 1.1 times the bar radius. The other values of the pattern speed were chosen around the middle one with a step size of $1.2 \text{ km s}^{-1} \text{ arcsec}^{-1}$.

All the mass models exhibit rather similar trends with changing pattern speed, so we demonstrate it only with model series M (Fig. 5). When the pattern speed rises, the nuclear ring becomes smaller. With the highest pattern speed, $\Omega_b = 9.8$, the inner ring disappears and the nuclear ring becomes very elongated and parallel with respect to the bar. The four-armed spiral structure can be seen clearly in models M5.5–M7.9. At both higher and lower pattern speeds, the spiral becomes two armed. Series D exhibits a four-armed structure in a narrower pattern speed range (D5.5–D6.9) and the arms are shorter and less sharp. In series H, the arms are very weak at all pattern speeds.

4.1.3 Miscellaneous parametric dependencies

We have also checked the effects of various other model parameters: the number of Fourier components that were used to calculate the gravitational potential, the bar turn-on speed, the collision frequency and the coefficient of restitution. All these have a smaller effect than the disc thickness or the pattern speed of the bar.

The inclusion of Fourier component $m = 4$ and the higher ones makes the four-armed spiral more pronounced. When only $m = 0$ and $m = 2$ components are included, the response is not a clear $m = 4$ spiral. We have also made simulations where we include the odd components of the Fourier decomposition. This causes some asymmetry to the models, especially in the region where spiral arms emerge from the inner ring.

We found that the bar turn-on speed can affect the innermost morphology: when the bar was turned on too abruptly (obtaining full strength in one or less bar rotation periods) some of the nuclear rings collapsed toward the centre or became very elongated and parallel to the bar. This is probably a result of the high amount of intersecting orbits. When the bar reached its full strength more gently (in two to four bar rotation periods), these gas particles were slowly ‘guided’ to orbits perpendicular with respect to the bar. However, when the pattern speed was high enough, even the gradual bar turn-on time could not save the nuclear rings, and the short-lived rings were destroyed before the bar reached its full strength.

We studied the effect of collision frequency by making selected simulations with different sizes and numbers of gas particles. If extreme values are ignored, the main morphological features are not strongly dependent on the collision frequency, which mainly affects the sharpness of features and their formation and evolution time-scale. The situation is quite similar with the coefficient of

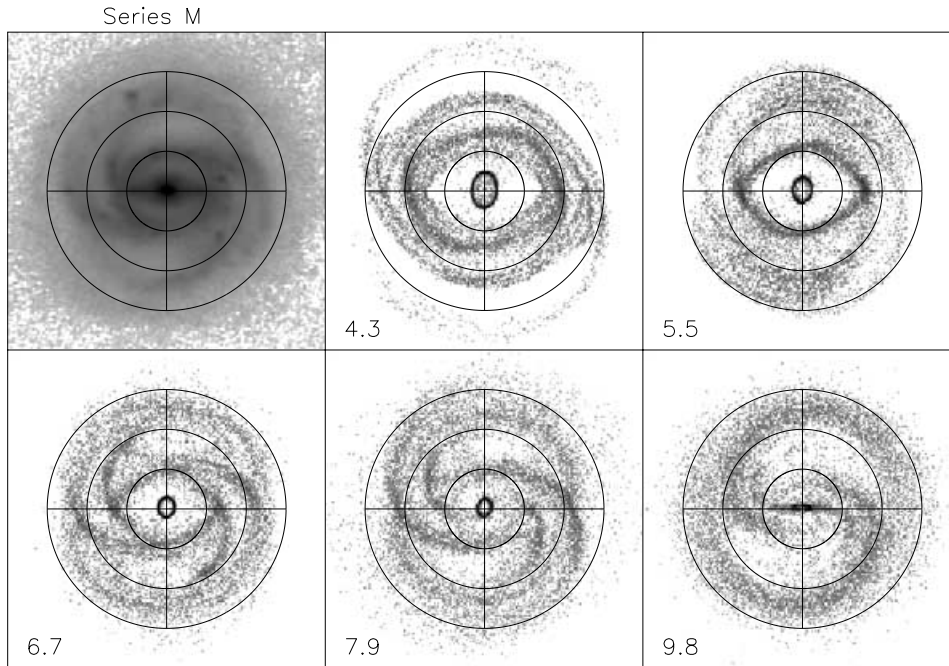


Figure 5. Pattern speed series for models with a moderate halo. The circles indicate radii of 15, 30 and 45 arcsec. The width of the frames is 120 arcsec. The models are shown one bar period after the bar has reached its full strength.

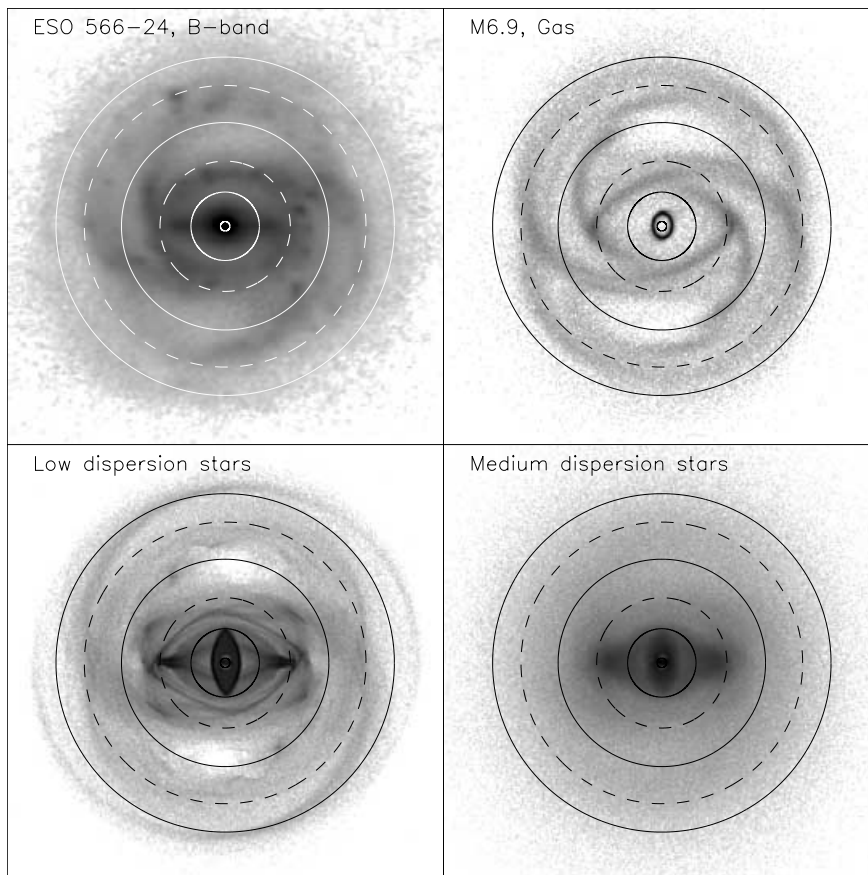


Figure 6. The top left-hand frame shows the resonance radii of model M6.9 plotted over the deprojected *B*-band image of ESO 566–24, in the top right-hand frame they are plotted over the gas morphology of the model. The bottom frames show the morphologies of two populations of non-colliding particles. The circles drawn with a continuous line show the radii of two ILRs, CR and OLR, whereas the circles drawn with a dashed line shows the inner and outer 4/1-resonance radii. To increase resolution, the simulation images are made by summing particle positions of 10 different time-steps after the bar has reached its full strength. The width of the frames is 120 arcsec.

restitution, α . Changing α between our standard value, 0.0, and about 0.5 has only a minor effect on the large-scale morphology: the spiral structure and the inner ring are sharper with lower values of α . Really high values, $\alpha > 0.6$, can be discarded because they produce a spiral structure that is too fuzzy. Nuclear rings are more sensitive to α and other collisional parameters. Higher values of α produce smaller and thicker rings. When α exceeds a certain limit (0.4–0.6, depending on other parameters, e.g. the collision frequency), the nuclear ring becomes very elongated and parallel with the bar. Shlosman & Noguchi (1993) found larger dependence on α , but in their models the gas component was self gravitating. In fact, our results are in accordance with their models with lowest gas fraction, where the inflow rate had weak or no dependence on the value of α (Table 2 in Shlosman & Noguchi 1993).

4.2 A search for the best fit

4.2.1 Morphology

The models without a halo have a problem with the positions of the four spiral arms: instead of a clear $m = 4$ spiral, the structure more resembles two pairs of arms, or doubled arms. Another, but smaller fault in series D is the lack of ‘morphological longevity’: the spiral structure disperses in just a few bar rotation periods. We can also discard series H, where the spiral arms are too weak. The models with a moderate halo, series M, exhibit an equally spaced and long-lasting spiral structure. Based on the overall fit of the spiral and ring morphology, our preferred model for further investigation is M6.7.

We have improved the pattern speed estimate by making several simulations around model M6.7. We derived $\Omega_b = 6.9 \pm 0.5 \text{ km s}^{-1} \text{ arcsec}^{-1}$, or about $33.7 \pm 2.3 \text{ km s}^{-1} \text{ kpc}^{-1}$. With this pattern speed, the locations of azimuthal density maxima closely coincide with the intensity maxima of the spiral arms, and also the radial extent of the arms corresponds to the observed one. The inner ring has a correct size, but it is slightly too pointed and elongated. Fig. 6 compares this

morphological best-fitting model M6.9 with the *B*-band morphology of ESO 566–24. The resonance radii corresponding the epicycle approximation are indicated as circles. The nuclear ring is between two ILRs (1.3 and 9.4'') and the inner ring is close to the inner 4/1 resonance (17.9''). The four-armed spiral structure is between the inner and outer 4/1 resonances (38.7''). The OLR radius (46.5 arcsec) is outside the spiral structure. The bar ends well before the CR radius (28.5''), near the inner 4/1 resonance. Using the bar radius of $18 \pm 2''$, this gives $r_{CR}/r_b = 1.58$. Combining the uncertainties in the determination of r_b and Ω_b , we finally get $r_{CR}/r_b = 1.6 \pm 0.3$.

The morphology of two populations of non-colliding test particles is also shown in Fig. 6. Both the low and the medium velocity dispersion components (initial velocity dispersion 1 and 30 per cent of the local circular velocity, respectively) have a strong contribution of orbits resembling closed x_2 -orbits (aligned perpendicular with respect to the bar) of analytical bar potentials (Contopoulos & Grosbøl 1989). Here, we call these orbits x_2 -like orbits instead of x_2 -orbits for two reasons. First, they are orbits of individual particles in our simulations, not exactly closed orbits found by iteration. Secondly, our bar is not an idealistic straight bar potential, because it is calculated from NIR photometry. In addition to x_2 -like orbits, the presence of x_1 -like orbits (aligned parallel with respect to the bar) can be seen in both populations. There is no support for a strong bar structure outside the inner 4/1 resonance, but in the medium dispersion case, there is a low-density oval with a minor-to-major axis ratio of about 0.5, that is aligned with the bar and reaches almost to corotation.

In Fig. 7 we compare the central morphology of low-dispersion collisionless populations in two different bar pattern speeds with the corresponding gas morphology and we also show some selected orbits of individual stellar particles. In model M6.9, there is a ‘stellar’ nuclear ring, which almost reaches the outer ILR radius of the epicycle approximation. The gaseous nuclear ring is considerably smaller. A possible reason for the size difference is that the outer x_2 -like orbits are crossing both a considerable population of x_1 -like

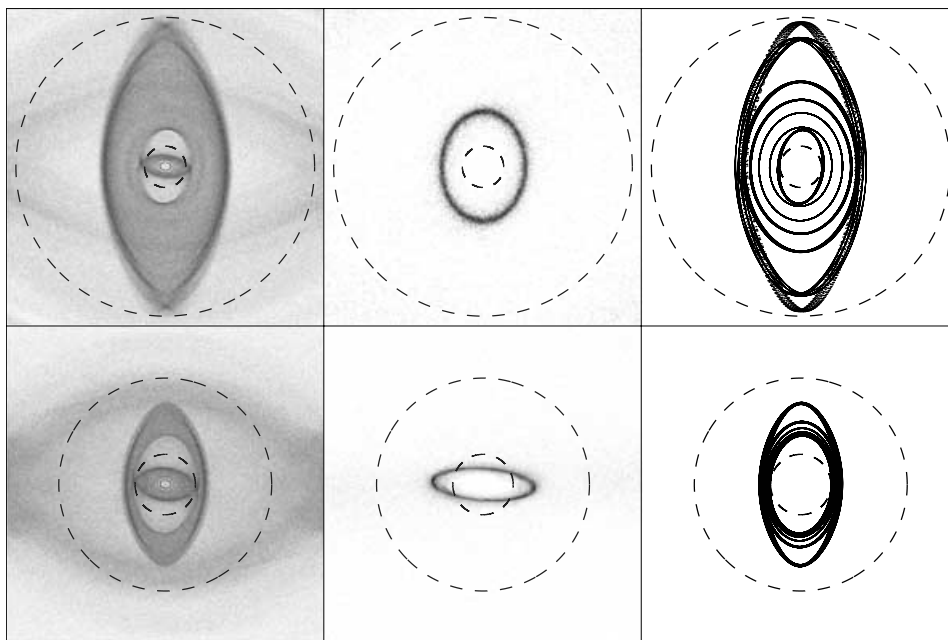


Figure 7. Stellar and gaseous nuclear rings versus x_2 -like orbits. The top row shows model M6.9, the left-hand frame shows the low-dispersion stellar particles, the middle frame the gaseous nuclear ring and the right frame selected stellar particle orbits. The bottom row shows the same for model M9.8. Outer and inner ILRs are indicated by circles drawn with a dashed line. The width of the frames is 20 arcsec.

orbits and other x_2 -like orbits. Colliding particles cannot stay on such orbits. Furthermore, the outermost orbits do not form closed loops, although they retain a perpendicular orientation with respect to the bar. The region suitable for non-crossing x_2 -like orbits corresponds quite well with the size of the gaseous nuclear ring. In model M9.8, the x_2 -like orbits do not reach as close to the linear outer ILR radius. Their domain is also much narrower, which could explain why the gaseous nuclear ring has the orientation of x_1 -like orbits.

We followed particle orbits in the region of the four-armed spiral and found a large number of particles librating around the Lagrangian points L_4 and L_5 (Binney & Tremaine 1987), which are close to the bar minor axis. However, the spiral structure cannot be explained by a single orbit type.

4.2.2 Kinematics

When modelling IC 4214, the fine details of the zero-velocity contour of the velocity field were valuable in determining the model parameters. Even though the non-axisymmetric perturbation in ESO 566–24 is considerably stronger than in IC 4214, the zero-velocity contour is rather featureless. This is owing to the unfavourable orientation of the bar with respect to the line of nodes. Alternatively, the ‘rotation curve’ constructed using the method introduced by Warner et al. (1973) shows the effect of non-circular velocities. Such features are clearest inside 10 arcsec, near the peak of Q_T , the relative non-axisymmetric force. Furthermore, the flatness of the outer rotation curve clearly indicates that at least some amount of halo is needed (supposing a constant M/L ratio).

Fig. 8 shows a comparison of selected rotation curves constructed from the modelled velocity field (data from 10 time-steps are summed) with the observed field. This velocity field does not have velocity information for the whole disc area, for example, the four-armed spiral structure is incompletely covered. On the other hand, many of our models include gas particles practically in the

whole disc area. To diminish this problem we adopted a density threshold to the modelled velocity field.

Our morphologically selected best-fitting model, M6.9 (Fig. 8a), gives a rather good fit with the position of the velocity jump near 10 arcsec. The inner parts also show a similar trend to the observed kinematics. However, the rotation amplitudes do not fit as well, the modelled velocity is too high inside 25 arcsec. A model with a thicker disc (Fig. 8b) gives a better fit, but the rotation amplitude inside 6 arcsec is still too high, by about 40 km s^{-1} . A considerable increase in Ω_b destroys the two-stage structure of the rising part of the rotation curve, as is highlighted by the kinematics of model M9.8 (Fig. 8c).

To get a better kinematical fit, we tried changing the relative masses of the bulge, disc and halo. In model B6.3 (Fig. 8d), where $(M/L)_B = 0.86$, $(M/L)_D = 1.02$ and $v_\infty = 219 \text{ km s}^{-1}$ we could get the difference between the inner velocities as low as $10\text{--}20 \text{ km s}^{-1}$. With the pattern speed at $6.3 \text{ km s}^{-1} \text{ arcsec}^{-1}$, which sets the inner 4/1 resonance to approximately the same distance as in model M6.9, the inner and nuclear rings are about the same size as in model M6.9. However, instead of four long spiral arms, we get several threaded arms. If we further decrease the relative contribution of the bulge, the nuclear ring changes its shape and orientation, by becoming dominated by x_1 -like orbits. As in model M9.8, the central kinematics shows a peak instead of a drop. Thus, based on the morphological and kinematical comparison, model M6.9 is our best-fitting solution for ESO 566–24.

The behaviour of the determined rotation curve inside 10 arcsec is related to the major axis of the bar being close to the kinematical minor axis. In the case of pure elliptical orbits with the major or minor axis being parallel to the kinematical major axis, the resulting rotation curve is either below (the major axis of the orbit is parallel to the kinematical major axis) or above (the minor axis of the orbit is parallel to the kinematical major axis) the local circular velocity (Teuben 2002). In barred galaxies, the shapes of orbits deviate from

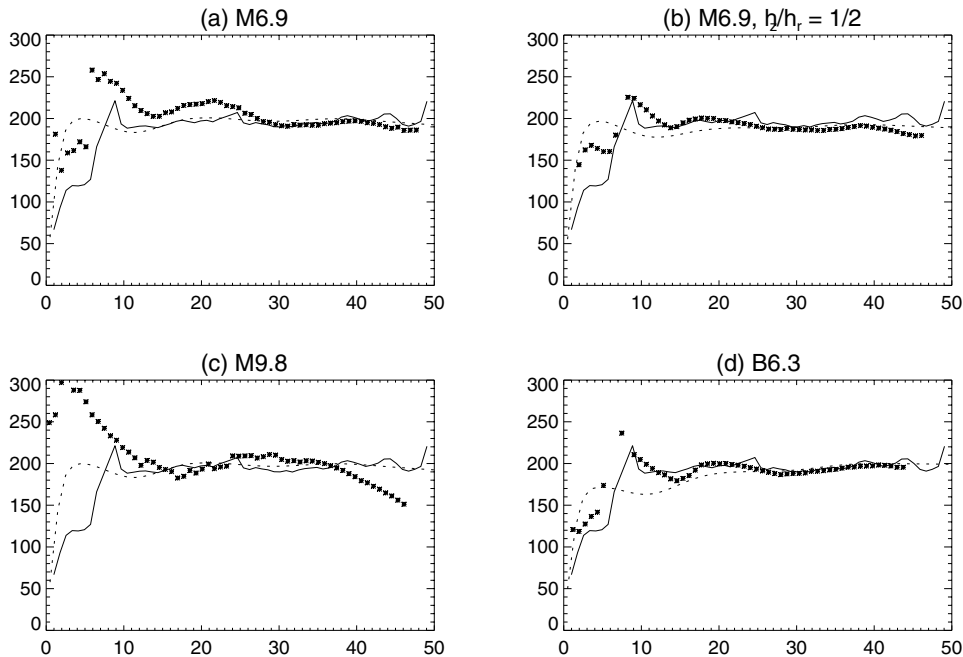


Figure 8. Comparison between the observed and modelled kinematics. The continuous line shows the observed ‘rotation curve’, derived from the velocity field. The dotted line shows the axisymmetric rotation curve based on the mass model and asterisk symbols show the simulated rotation curve constructed in the same way as the one observed.

pure ellipses, but this approximation is still helpful in understanding the kinematics of ESO 566–24.

Now, the low velocities in the region inside 6 arcsec are caused by x_2 -like orbits. The velocity of these orbits near the bar minor axis (the major axis of the orbits), is much lower than the local circular velocity. This is also close to the kinematical major axis, and thus the determined rotation curve in this region is below the axisymmetric rotation curve calculated from the mass distribution. Similarly, the velocity peak near 10 arcsec is caused by x_1 -like orbits, which are parallel to the bar. In this distance, they are near their minor axis, and the velocity is higher than the local circular velocity. The radial location of the velocity peak depends on the extent of the x_2 -like gas particle orbits.

5 DISCUSSION

5.1 Spiral morphology in barred galaxies

A classic case of a barred spiral galaxy is NGC 1300, where a two-armed spiral structure starts from the ends of the bar. Quite often, the spiral arms emerge from an inner ring that surrounds the bar. There are also cases where the spiral arms start offset with respect to the ends of the bar. This can happen both in the leading and trailing quadrants of the bar. A two-armed grand design structure is not the only possibility in barred galaxies. Different kinds of arm multiplicities also exist: arm bifurcation at large radius, doubled arms (one or both), and even genuine multiple-arm structures. Flocculent barred galaxies are rare but known (Buta 1995). According to Elmegreen & Elmegreen (1995), the length of the two-armed phase correlates with the bar length: it reaches about twice the bar radius.

There are cases where the multiple-arm or flocculent spiral morphology of visual images disappears and a two-armed grand design spiral emerges in the NIR (Block & Wainscoat 1991; Block, Elmegreen & Wainscoat 1996; Block et al. 1999). It has been claimed that this kind of dualistic morphology is universal (Block & Puerari 1999). However, the study by Eskridge et al. (2002), based on the Ohio State University Bright Galaxy Survey (OSU survey), includes several barred galaxies where the multiple-arm structure is also seen in the NIR images. The examples include all variations of multiplicities from arm bifurcations to arm doublings and genuine multiple-armed spirals. For example, there is a three-armed spiral galaxy, NGC 5054 (another example is NGC 7137; Grosbøl & Patsis 1999). Although there are four-armed galaxies in the OSU sample, none of them have a regular $m = 4$ structure as observed in ESO 566–24.

ESO 566–24 with its very regular four-armed spiral structure is really exceptional. The four arms have roughly the same length, so they do not appear to have formed as a bifurcation of a usual two-armed structure. Furthermore, they are so far from each other (at 35 arcsec, the phase difference between the arms is about 90°), that arm doubling is clearly not the case. To crown the status of ESO 566–24 as a genuine $m = 4$ spiral, the arms also have comparable strength in the NIR. In the OSU survey, the galaxy with the closest resemblance to ESO 566–24 is NGC 613. It has altogether five spiral arms, but the ‘extra’ arms are not as strong and regular as in ESO 566–24.

Some barred galaxies have features called plumes, i.e. short arcs besides the main spiral arms in the leading side with respect to the bar (Buta 1984). The best-known case is NGC 1433 (Buta 1986; Ryder et al. 1996). It is possible that plumes could be related to a four-armed spiral structure, for example, they could be remnants of additional spiral arms. However, such features can form in gas

dynamical simulations as result of doubled spiral arms (Byrd et al. 1994). It would be interesting to thoroughly compare ESO 566–24 with NGC 1433.

Our models can reproduce the four-armed spiral rather well, and set constraints to essential model parameters, but they do not directly unveil the origin of this structure. In the best case, our models are snapshots of the current stage of the evolution of ESO 566–24. It is possible that the location of resonances can give a clue to the origin of the four-armed spiral; it seems that this structure is approximately confined between inner and outer 4/1 resonances. Thus the situation could be analogous to two-armed spirals, which are sometimes suggested to end near the OLR (e.g. Elmegreen et al. 1989). Note, however, that at least for non-barred galaxies, other solutions have also been suggested (Patsis et al. 1994; Patsis, Grosbøl 1997).

We have one N -body example, which exhibits a short-lived regular four-armed spiral with a lifetime less than one bar rotation period. This takes place when the bar is still quickly strengthening and growing. This N -body simulation was not intended to model ESO 566–24, but we mention it because a possibility to be considered is that the four-armed spiral structure could represent a short-lived transient stage in galactic evolution. Then its rarity would not require a strictly limited location in parameter space.

5.2 Rings

The inner ring in our best-fitting model is in accordance with most studies on ring formation in barred galaxies (Schwarz 1981, 1984a,b; Combes & Gerin 1985; Byrd et al. 1994; Rautiainen & Salo 2000): its major axis is close to inner 4/1 resonance. The nuclear rings have often been identified with x_2 orbits, which are perpendicular to the bar. When the non-axisymmetric perturbation is weak, the outermost stable x_2 orbits reach the ILR (or the outer ILR) (Contopoulos & Grosbøl 1989). However, when the strength of the perturbation is increased, the linear approximation is not valid, and the extent of the x_2 orbits moves inwards. A further complication is that the gas accumulation into a nuclear ring can change the gravitational potential and have a strong effect on orbits near the outer ILR (Heller & Shlosman 1996).

Recently, Regan & Teuben (2003) have suggested that the nuclear rings are not related to resonances, but instead they form as an interaction between gas flows along x_2 - and x_1 -like streamlines. Furthermore, the nuclear rings in their hydrodynamic models shrank throughout the simulation. This also happens in our simulations, but the change in the ring size is very slow in the later phases, possibly owing to depopulation of the nearest x_1 -like orbits. We did not find the interaction of two different gas streamlines necessary for the nuclear ring formation. A clear ring also formed when all the particles initially resided in the domain of x_2 -like orbits. In fact, a ring formed even without gas: a rotating bar can redistribute non-colliding particles near the outermost x_2 -like orbits. Rings can also form in self-gravitating stellar particles of N -body simulations (Rautiainen & Salo 2000; Athanassoula & Misiriotis 2002). In ESO 566–24, the inner ring is clearly present in the H -band, and corresponding examples also exist for outer and nuclear rings. Thus, it seems that a ring can also form as a response of the old stellar population to a non-axisymmetric potential.

When taking into account the previously mentioned sensitivity to collisional parameters and the relatively small size of the nuclear ring (a_{nr} is about 4 pixels of the H -band image), it is questionable whether the morphology of the nuclear ring can be used as a constraint of the model parameters.

5.3 Pattern speed dilemma

Our best-fitting models place the CR at about 1.6 times the bar radius. This is considerably larger than the often-cited value of $r_{\text{CR}}/r_b = 1.2 \pm 0.2$. For IC 4214 we found a value of 1.4 ± 0.2 (Salo et al. 1999), thus just barely fitting within the fast bar regime although it has an early-type morphology. This raises a question if our modelling method is biased so that it gives values that are too high. Our preliminary results with other galaxies suggest otherwise; for example, for NGC 4314 we get r_{CR}/r_b close to 1.

We extended a previous study by Elmegreen (1996) by a brief search of the literature. We found pattern speed determinations of individual barred galaxies in the range $0.77 \leq r_{\text{CR}}/r_b \leq 2.4$, the average value being about 1.35 (the median value was 1.3). The values based on the Tremaine–Weinberg method tend to be close to 1, although Aguerri et al. (2003) found higher values for galaxies NGC 1440 ($1.6^{+0.5}_{-0.3}$) and NGC 3412 ($1.5^{+0.6}_{-0.3}$). ESO 566–24 is of Hubble type SB(r)b, later than most galaxies whose pattern speed has been determined with the Tremaine–Weinberg method (typically SB0). Elmegreen & Elmegreen (1985) have suggested that early-type galaxies have longer bars than late-type galaxies in both the physical size and with respect to resonance locations. Thus, the high value of r_{CR}/r_b found in our study could be related to physical conditions which correlate with the Hubble type.

An often-mentioned point in favour of higher pattern speeds is the shapes of dust lanes inside the bar. According to Athanassoula (1992) the offset dust lanes form when the galaxy has an ILR and their shape corresponds to the observations when $r_{\text{CR}} = 1.2 \pm 0.2 r_b$. However, the dust-lane argument for fast bars may not be as strong as it seems: Lindblad & Kristen (1996) found two possible pattern speeds for NGC 1300, giving $r_{\text{CR}}/r_b = 1.3$ and $r_{\text{CR}}/r_b = 2.4$, both producing good dust-lane morphology.

N -body studies have shown that pattern speeds of the bar and spiral arms can be different, the structures being either separate or in a non-linear mode coupling (Sellwood & Sparke 1988; Masset & Tagger 1997; Rautiainen & Salo 1999). The presence of two strong modes can induce cyclic evolution in the shape and orientation of the rings (Rautiainen & Salo 2000; Rautiainen et al. 2002). In principle, ESO 566–24 could be modelled with two modes: the inner region having a higher pattern speed and the four-armed spiral a pattern speed in the range of our single pattern models. However, our low value for Ω_b is based not only on the modelling of the four-armed spiral structure, but the inner and nuclear rings also have approximately the right size with this pattern speed.

5.4 Halo contribution

Interaction between the bar and dark halo can introduce bar slowdown that cannot be compensated by bar growth. Weinberg (1985) studied the dynamical friction between a bar and halo analytically and by a semi-restricted N -body simulation, and found that it causes the bar to lose most of its angular momentum in just a few bar rotations. Little & Carlberg (1991) studied bar slowdown by self-gravitating N -body models, where both the disc and halo were two dimensional. The bar deceleration in their model was considerably lower, only by a factor of 2 during 10 Gyr, half of which was owing to the interaction with the outer disc. Alternatively, Hernquist & Weinberg (1992) who used an analytical bar with a self-gravitating halo, found a high slowdown rate.

Debatista & Sellwood (1998, 2000), who made fully consistent N -body simulations, found that in models with centrally concentrated haloes, the bar slows down dramatically ($r_{\text{CR}}/r_b > 1.4$), un-

less the halo has an unrealistically high angular momentum in the same direction as the disc. Valenzuela & Klypin (2003) who used adaptive grid refinement to increase the gravity resolution, found that the bar pattern speed was almost constant and that the stellar disc lost only 5–10 per cent of its angular momentum to the halo. Recently, Athanassoula (2003) showed that the bar pattern speed is difficult to be used as an argument for either high or low halo-to-disc mass ratios: when the halo or disc-velocity dispersion is increased, the bar slowdown rate also decreases.

Anyhow, if we compare our best-fitting mass model with the simulations of Debatista & Sellwood (1998) with a non-rotating halo, and adopt their parameter $\eta = (v_{\text{disc}}/v_{\text{halo}})^2$ at the maximum of the disc rotation curve, we find $\eta = 3.65$. In their fig. 2, this would correspond to $r_{\text{CR}}/r_b = 1.3 - 1.4$ at the final equilibrium state. Alternatively, if we include a bulge to v_{halo} , we get $\eta = 1.39$, corresponding to $r_{\text{CR}}/r_b > 2$. Debatista & Sellwood (2000) found that a halo which rotates in the same sense as the bar can induce a lower bar slowdown rate than non-rotating or retrograde haloes. Taking into account possible bulge rotation, our result $r_{\text{CR}}/r_b \approx 1.6$ is not in disagreement with their results. However, the situation is the same with Valenzuela & Klypin (2003); in their models $r_{\text{CR}} = 1.2-1.7 r_b$.

In our best-fitting model (M6.9), the dark halo contributes less than 20 per cent of the mass inside $r_{2.2}$. The rotation curve is dominated by luminous matter inside the whole disc region. Thus, our favoured halo component for ESO 566–24 is close to the predicted URC halo (Persic et al. 1996), and our results are in agreement with (Salucci & Persic 1999). This is also in accordance with estimates of disc mass contribution by dynamical modelling (e.g. Weiner, Sellwood & Williams 2001), but disagrees with cold dark matter cosmological N -body simulations, which produce cuspy haloes (e.g. Navarro, Frenk & White 1996).

6 CONCLUSIONS

We have constructed models for the four-armed barred spiral galaxy ESO 566–24. The mass distribution of the different components is based on NIR photometry with the exception of a dark halo, whose amount was chosen to fit the rotation curve at large radii. Our best-fitting model reproduces the observed four-armed morphology. In addition, the kinematic characteristics of our model resemble those observed. The main conclusions are as follows.

(i) Two major factors affecting the simulated morphology and kinematics are the strength of the non-axisymmetric perturbation and the pattern speed of the bar. The former depends on the mass and the thickness of the disc.

(ii) Both the kinematical and morphological fits are better when a moderate halo component is included. Alternatively, a dominating halo can be ruled out, because then the gas response to the disc gravitational potential is too weak. Thus, the contribution of the luminous matter dominates the rotation curve inside the whole region of the optical disc.

(iii) The four-armed spiral could be produced between the inner and outer 4/1 resonances. The inner ring is close to the inner 4/1 resonance and the nuclear ring is between two ILRs. The size of the nuclear ring seems to correlate with the size of the region suitable for non-crossing x_2 -like orbits.

(iv) If the bar has the same pattern speed as the four-armed spiral, then it rotates rather slowly; the corotation radius is about 1.6 ± 0.3 times r_b , which is higher than the often-cited value of 1.2 ± 0.2 . A possible reason for this discrepancy may be that most bar pattern

speed determinations have been made for galaxies of earlier Hubble type than ESO 566–24.

(v) The rather high value of $r_{\text{CR}}/r_{\text{b}}$ is difficult to be disputed by pattern speed multiplicity. In addition to the spiral structure, the nuclear and inner rings can be reproduced in the right scale with a single pattern speed. Adopting higher pattern speeds, which would be consistent with the bar ending near corotation, produce significantly worse-fitting ring morphology. Also, the kinematics of the central parts deviate more from the observed velocities.

(vi) The relatively slow bar rotation rate can be as a result of interaction between the bar and the spheroidal component (halo and bulge). The exceptional $m = 4$ spiral morphology can be related to the low bar rotation rate and the importance of the spheroidal component.

(vii) The curious shape of the inner rotation curve can be explained by the combined effects of x_1 - and x_2 -like orbits.

ACKNOWLEDGMENTS

We thank an anonymous referee for comments, which helped us to improve the manuscript. We also thank P. Salucci and V. Debattista for their comments. This work has been supported by the Väisälä Foundation and by the Academy of Finland. RB acknowledges the support of NSF grant AST-0205143 to the University of Alabama. This work made use of data from the Ohio State University Bright Spiral Galaxy Survey, which was funded by grants AST-9217716 and AST-9617006 from the United States National Science Foundation, with additional support from the Ohio State University.

REFERENCES

- Agueri J. A. L., Debattista V. P., Corsini E. M., 2003, *MNRAS*, 338, 465
 Athanassoula E., 1992, *MNRAS*, 259, 345
 Athanassoula E., 2003, *MNRAS*, 341, 1179
 Athanassoula E., Misiriotis A., 2002, *MNRAS*, 330, 35
 Binney J., Tremaine S., 1987, *Galactic Dynamics*. Princeton Univ. Press, Princeton NJ
 Block D. L., Puerari I., 1999, *A&A*, 342, 627
 Block D. L., Wainscoat R. J., 1991, *Nat*, 353, 48
 Block D. L., Elmegreen B. G., Wainscoat R. J., 1996, *Nat*, 381, 674
 Block D. L., Puerari I., Frogel J. A., Eskridge P. B., Stockton A., Fuchs B., 1999, *Ap&SS*, 269, 5
 Buta R., 1984, *Publ. Astron. Soc. Australia*, 5, 472
 Buta R., 1986, *ApJS*, 61, 631
 Buta R., 1988, *ApJS*, 66, 233
 Buta R., 1995, *ApJS*, 96, 39
 Buta R., Block D. L., 2001, *ApJ*, 550, 243
 Buta R., Combes F., 1996, *Fundamentals Cosmic Phys.*, 17, 95
 Buta R., Combes F., 2000, in Combes F., Mamon G. A., Charmandaris V., eds, *ASP Conf. Ser. Vol. 197, Dynamics of Galaxies: from the Early Universe to the Present*. Astron. Soc. Pac., San Francisco, p. 11
 Buta R., Crocker D. A., 1991, *AJ*, 102, 1715
 Buta R., Crocker D. A., 1993, *AJ*, 105, 1344
 Buta R., Purcell G. B., 1998, *AJ*, 115, 484
 Buta R., Alpert A. J., Cobb M. L., Crocker D. A., Purcell G. B., 1998, *AJ*, 116, 1142
 Buta R., Purcell G. B., Cobb M. L., Crocker D. A., Rautiainen P., Salo H., 1999, *AJ*, 117, 778
 Buta R., Ryder S. D., Madsen G. J., Wesson K., Crocker D. A., Combes F., 2001, *AJ*, 121, 225
 Byrd G., Rautiainen P., Salo H., Buta R., Crocker D. A., 1994, *AJ*, 108, 476
 Canzian B., 1993, *ApJ*, 414, 487
 Canzian B., Allen R. J., 1997, *ApJ*, 479, 723
 Combes F., Gerin M., 1985, *A&A*, 150, 327
 Combes F., Sanders R. H., 1981, *A&A*, 96, 164
 Contopoulos G., Grosbøl P., 1989, *A&AR*, 1, 261
 de Grijs R., 1998, *MNRAS*, 299, 595
 de Grijs R., Peletier R. F., van der Kruit P. C., 1997, *A&A*, 327, 966
 Debattista V. P., Sellwood J. A., 1998, *ApJ*, 493, L5
 Debattista V. P., Sellwood J. A., 2000, *ApJ*, 543, 704
 Duval M. F., Athanassoula E., 1983, *A&A*, 121, 297
 Elmegreen B., 1996, in Buta R., Crocker D. A., Elmegreen B. G., eds, *ASP Conf. Ser. Vol. 91, Barred Galaxies*, IAU Colloquium 157. Astron. Soc. Pac., San Francisco, p. 197
 Elmegreen B. G., Elmegreen D. M., 1985, *ApJ*, 288, 438
 Elmegreen B. G., Seiden P. E., Elmegreen D. M., 1989, *ApJ*, 343, 602
 Elmegreen D. M., Elmegreen B. G., 1995, *ApJ*, 445, 591
 Eskridge P. B. et al., 2000, *AJ*, 119, 536
 Eskridge P. B. et al., 2002, *ApJS*, 143, 73
 Grosbøl P. J., Patsis P. A., 1999, in Merritt D., Sellwood J. A., Valluri M., eds, *ASP Conf. Ser. Vol. 182, Galaxy Dynamics: A Rutgers Symposium*. Astron. Soc. Pac., San Francisco, p. 217
 Heller C. H., Shlosman I., 1996, *ApJ*, 471, 143
 Hernquist L., Weinberg M. D., 1992, *ApJ*, 400, 80
 Kent S. M., 1986, *AJ*, 91, 1301
 Kent S. M., 1987, *AJ*, 93, 1062
 Knapen J. H., Shlosman I., Peletier R. F., 2000, *ApJ*, 529, 93
 Laurikainen E., Salo H., 2002, *MNRAS*, 337, 1118
 Laurikainen E., Salo H., Rautiainen P., 2002, *MNRAS*, 331, 880
 Lindblad P. A. B., Kristen H., 1996, *A&A*, 313, 733
 Lindblad P. A. B., Lindblad P. O., Athanassoula E., 1996, *A&A*, 313, 65
 Little B., Carlberg R. G., 1991, *MNRAS*, 250, 161
 Maoz D., Barth A. J., Sternberg A., Filippenko A. V., Ho L. C., Macchetto F. D., Rix H., Schneider D. P., 1996, *AJ*, 111, 2248
 Masset F., Tagger M., 1997, *A&A*, 322, 442
 Merrifield M. R., Kuijken K., 1995, *MNRAS*, 274, 933
 Navarro J. F., Frenk C. S., White S. D. M., 1996, *ApJ*, 462, 563
 Patsis P. A., Hiortel N., Contopoulos G., Grosbøl P., 1994, *A&A*, 286, 46
 Patsis P. A., Grosbøl P., Hiortel N., 1997, *A&A*, 323, 762
 Persic M., Salucci P., Stel F., 1996, *MNRAS*, 281, 27
 Purcell G. B., 1998, PhD thesis, Univ. Alabama
 Rautiainen P., Salo H., 1999, *A&A*, 348, 737
 Rautiainen P., Salo H., 2000, *A&A*, 362, 465
 Rautiainen P., Salo H., Laurikainen E., 2002, *MNRAS*, 337, 1233
 Regan M. W., Teuben P., 2003, *ApJ*, 582, 723
 Rix H., Rieke M. J., 1993, *ApJ*, 418, 123
 Ryder S. D., Buta R. J., Toledo H., Shukla H., Staveley-Smith L., Walsh W., 1996, *ApJ*, 460, 665
 Sackett P. D., 1997, *ApJ*, 483, 103
 Salo H., Rautiainen P., Buta R., Purcell G. B., Cobb M. L., Crocker D. A., Laurikainen E., 1999, *AJ*, 117, 792
 Salucci P., Persic M., 1999, *A&A*, 351, 442
 Schwarz M. P., 1981, *ApJ*, 247, 77
 Schwarz M. P., 1984a, *MNRAS*, 209, 93
 Schwarz M. P., 1984b, *A&A*, 133, 222
 Sellwood J. A., 1981, *A&A*, 99, 362
 Sellwood J. A., Sparke L. S., 1988, *MNRAS*, 231, 25p
 Sempere M. J., Garcia-Burillo S., Combes F., Knapen J. H., 1995, *A&A*, 296, 45
 Shlosman I., Noguchi M., 1993, *ApJ*, 414, 474
 Teuben P. J., 2002, in Athanassoula E., Bosma A., Mujica R., eds, *ASP Conf. Ser. Vol. 275, Discs of Galaxies: Kinematics, Dynamics and Perturbations*. Astron. Soc. Pac., San Francisco, p. 217
 Tremaine S., Weinberg M. D., 1984, *ApJ*, 282, L5
 Valenzuela O., Klypin A., 2003, *MNRAS*, 345, 406
 Warner P. J., Wright M. C. H., Baldwin J. E., 1973, *MNRAS*, 163, 163
 Weinberg M. D., 1985, *MNRAS*, 213, 451
 Weiner B. J., Sellwood J. A., Williams T. B., 2001, *ApJ*, 546, 931

This paper has been typeset from a $\text{\TeX}/\text{\LaTeX}$ file prepared by the author.